Transcranial photoacoustic imaging of NMDA-evoked focal circuit dynamics in rat forebrain

Jeeun Kang[1,2], Shilpa D. Kadam[3], Joshua S. Elmore[1], Brennan J. Sullivan[4], Heather Valentine[1], Adarsha P. Malla[5], Anthony A. Grace[6], Arman Rahmim[1], Leslie M. Loew[7], Michael Baumann[8], Albert Gjedde[1,9,10,11], Emad M. Boctor[1,2], Dean F. Wong[5, 12, 13, *]

[1] Russell H. Morgan Department of Radiology and Radiological Science, Johns Hopkins University, Baltimore, MD, USA.

[2] Laboratory of Computational Sensing and Robotics, Whiting School of Engineering, Johns Hopkins University, Baltimore, MD, USA

[3] Neuroscience Laboratory, Hugo W. Moser Research Institute at Kennedy Krieger & Department of Neurology, Johns Hopkins Medical Institutions, Baltimore, MD, USA

[4] Neuroscience Laboratory, Hugo W. Moser Research Institute at Kennedy Krieger, Baltimore, MD, USA

[5] Solomon H. Snyder Department of Neuroscience, Johns Hopkins Medical Institutions, Baltimore, MD, USA

[6] Departments of Neuroscience, Psychiatry and Psychology, University of Pittsburgh, Pittsburgh, PA, USA

[7] Department of Cell Biology, University of Connecticut Health, Farmington, CT, USA

[8] National Institute on Drug Abuse, Intramural Research Program, NIH, Baltimore, MD

[9] Departments of Clinical Research and Nuclear Medicine, Odense University Hospital and University of Southern Denmark, Odense, Denmark

[10] Department of Neurology and Neurosurgery, McGill University, Montreal, Quebec, Canada

[11] Department of Neuroscience, University of Copenhagen, Copenhagen, Denmark

[12] Department of Psychiatry and Behavioral Sciences, Johns Hopkins Medical Institutions, Baltimore, MD, USA

[13] Department of Neurology, Johns Hopkins Medical Institutions, Baltimore, MD, USA.

*** Correspondence:**
Dean F. Wong
dfwong@jhmi.edu

Keywords: Photoacoustic, neuroimaging, voltage-sensitive dye imaging, microdialysis, quantitative encephalopathy, N-methyl-D-aspartate, glutamate, motor cortex, hippocampus.

Abstract

Transcranial photoacoustic (PA) voltage-sensitive dye (VSD) imaging promises to overcome current temporal and spatial limitations of functional neuroimaging. The technique previously distinguished global seizure activity from control neural activity in groups of rats. To validate the focal specificity of transcranial PA with VSD (IR780) imaging *in vivo*, we now present proofs-of-concept that the results differentiate between N-methyl-D-aspartate (NMDA) evoked neural activities in two distinct circuits with differential response profiles, i.e., sensorimotor cortex and hippocampus. Concurrent quantitative EEG (qEEG) recorded real time circuit dynamics. We hypothesized that NMDA evoked focal glutamate release in both circuits would correlate with increases of location-specific PA signals and time-specific EEG signals. To test the hypothesis in hippocampus 0.3, 1 and 3 mM NMDA was infused at a rate of 2 μl/min over 60 min via an implanted microdialysis probe. The dialysate samples collected every 20 minutes during the infusion were analyzed for focal changes in extracellular glutamate release and quantified by high-performance liquid chromatography (HPLC). Microdialysis at 0.3, 1 and 3 mM showed dose-dependent increases of glutamate (39%, 200% and 670 %, respectively) in hippocampus. We recorded dose-dependent increases of the PA signal with 0.3 and 3 mM NMDA infusion as predicted. Recorded qEEG at 3 mM NMDA infusion confirmed induction of focal seizure activity. Transcranial PA VSD imaging provided up to 301.45 ± 42.48 % of fractional neural activity index change measured at contralateral side of microdialysis probe with 3 mM NMDA infusion, while -24.48 ± 34.16 % of fractional decrease with 0.3 mM NMDA infusion. This clearly suggests function of dentate gyrus (DG) gatekeeping in hippocampus. When we tested the hypothesis in sensorimotor cortex, intracerebral infusion of NMDA at 0.3 mM elicited the predicted increase of glutamate release, with an unexpected decrease of qEEG spectral power; suggesting surround inhibition due to preferential activation of inhibitory interneurons. Transcranial PA VSD imaging had -13.22 ± 37.08 % of fractional neural activity index change during 20 min of 0.3 mM NMDA infusion, consistent with surround suppression of depolarization as shown by qEEG of motor cortex. Therefore, transcranial PA VSD imaging distinguished cortical surround inhibition and hippocampal focal seizure activity that correlated with activities reported by qEEG signals with similar protocols. The results show this emerging technology to be an innovative and significant advance of functional neuroimaging.

1 Introduction

Whereas electrophysiological and invasive neurochemical techniques have been valuable in assessing activity within specific neural circuits in brain, there is a distinct need for a noninvasive means to image real-time regional functional activity in vivo. In particular, motor cortex and hippocampus are of interest, as they present distinct circuits with clear electrophysiological with respect to the modulation of excitatory neurotransmission. It is long known that neocortical structures such as the motor cortex exhibit both excitatory and concomitant strong surround physiological inhibitory mechanisms that focus neuronal activity, where activation needs to remain focused to a small cortical area to achieve fine sensory-motor control (Sachdev et al., 2012). The focal application of low doses of NMDA is proposed to activate "spreading-depression", an electrophysiological process that is dependent upon NMDA receptors (Marrannes et al., 1988). Previous optical imaging approaches of the cortical surround suppression (Petersen and Sakmann, 2001; Derdikman et al., 2003; Petersen et al., 2003) were accomplished with invasive procedures to overcome superficial imaging depth, and further extension to deeper brain regions such as the hippocampus were prohibitive. In contrast, the hippocampal circuit, which is the seat of learning and memory, has rows of excitatory pyramidal neurons all aligned in close-proximity and similar orientation in the dentate gyrus (DG) that sit at a negative hyperpolarized resting membrane potential that form the putative "gating" for signals incoming from adjacent cortices. Low amplitude excitatory inputs are unable to depolarize the DG neurons and therefor fail to "open" the DG gate (Andersen et al., 1966). However, once a strong and repetitive signal successfully depolarizes DG neurons, the simultaneous firing of action potentials leads to giant excitatory postsynaptic potentials (EPSPs) (Andersen et al., 1966). This all-or-none gating system in the DG is therefore distinct in its circuit dynamics from the motor cortex. The imaging of glutamate dynamics within the hippocampus have been primarily accomplished by optical imaging of freshly-sliced brain tissue (Okubo et al., 2010) or magnetic resonance imaging spectroscopy (MRS) providing non-invasive quantification of glutamate at high spatial resolution (Crescenzi et al., 2017; Voets et al., 2017). However, optical imaging and MRS suffer from the need to isolate brain tissue ex vivo and slow imaging speed, respectively. Another approach using two-photon microscopy to measure calcium ion dynamics in various deep brain structures including the hippocampus does not provide temporal resolution in real-time. (Kondo et al., 2017) Therefore, non-invasive, real-time visualization with spatiotemporal resolution would be a significant advance; however, such an approach would require neurochemical and electrophysiological validation to help better characterize the neural activity recorded via EEG.

Photoacoustic (PA) imaging is a hybrid modality between optics and acoustics that provides a molecular signature to the neural activity assessed via acoustic transcranial imaging (Wang et al., 2003; Wang and Hu, 2012). PA imaging is based on thermo-elastic perturbation of a target evoked by light absorbance from a pulsed laser illumination, which generates radio-frequency (RF) acoustic pressure that is detected by a piezoelectric ultrasound transducer or optical interferometer. From this unique imaging mechanism, several attractive applications have been proposed in preclinical and clinical researches using tomographic and microscopic imaging modes, such as detecting endogenous contrast of cancer indicators (e.g., melanoma (Zhang et al., 2006), breast microcalcifications (Kang et al., 2014; Kim et al., 2014; Kang et al., 2015)), monitoring of cancer angiogenesis (Yao et al., 2012), oxygen metabolism (Hu, 2016), and quantification of lipid content (Hui et al., 2017; Wu et al., 2017), among others. Recently the application of PA imaging is being expanded to neuroscience (Nie et al., 2012; Liu et al., 2017; Li et al., 2018): Label-free transcranial PA imaging of neurovascular coupling has been proposed as a means to quantify hemodynamic changes (Hu and Wang, 2010; Zhang et al., 2018); however this approach is not capable of quantifying neural activities that directly correspond to neural electrical activity, which is required for the proposed imaging of the distinct neural mechanisms within motor cortex and hippocampus. In addition to hemoglobin, which can provide an effective contrast signal, there has been extensive investigations into more effective exogenous contrast agents (Luke et al., 2011; Huynh et al.,

2014; Moon et al., 2015; Ju et al., 2016; Weber et al., 2016), and several PA approaches have been capable of detecting electrophysiological neural activities using functional voltage sensors. Deán-Ben et al. showed real-time PA tomography of a genetically encoded calcium indicator, GCaMP5G, using zebrafish *in vivo* (Deán-Ben et al., 2016). Sheryl Roberts, et al. also proposed a new metallochromic calcium sensor for PA imaging (CaSPA) which has a high extinction coefficient, a low quantum yield, and high photo-bleaching resistance for brain and heart imaging (Roberts et al., 2018). Ruo et al. reported PA imaging of neural activity evoked by electrical stimulation and 4-aminopyridine-induced epileptic seizures using hydrophobic anions such as dipicrylamine (DPA) in mouse brain.(Rao et al., 2017) However, these voltage sensors requires PA imaging at the visible spectral range (488 nm and 530 nm for GCaMP5G; 550 nm for CaSPA; 500 nm and 570 nm for DPA), which is suboptimal for deep neural activity imaging due to an inevitable optical attenuation produced by blood absorption of the signal. Also, imaging within the intact brain requires sufficient resolution to assess activity within the hippocampus at approximately 5 mm - 8 mm of imaging depth including scalp and cortex regions for the rat (Nowak et al., 2011; Paxinos and Watson, 2014) Recently, we proposed transcranial PA recordings of brain activity *in vivo* with a near-infrared voltage-sensitive dye (VSD, 790 nm), delivered through the blood-brain barrier (BBB) via pharmacological modulation, as a promising tool to transcend current functional neuroimaging limitations, particularly as it relates to sensing depth (Kang et al., 2017; Zhang et al., 2017). The studies demonstrated the ability of transcranial PA imaging of near-infrared VSD to distinguish *in vivo* seizure activity in the rat brain from control groups in real time (Kang et al., 2017). However, these results are limited by the use of a global chemoconvulsant, causing perturbation across the entire brain caused by the intraperitoneal administration of penetylenetetrazole (PTZ). Therefore, further advances require imaging focal neural stimulation of heterogeneous neural circuits, with concomitant validation from other validated neuroscience methodologies.

In this study, we validate *in vivo* transcranial PA neuroimaging of distinct neural circuit mechanisms both activated via stimulation of N-methyl-D-aspartate (NMDA) receptors in motor cortex and hippocampus in vivo in rat brain through an intact skull and scalp. This tri-modal neural sensing approach using microdialysis, quantitative electroencephalography (qEEG), and transcranial PA imaging enables simultaneous monitoring of neurochemical and electrophysiological changes in neural activity and associated glutamatergic neurotransmission (Figure 1a). The controlled stimulation of these circuits was conducted by reverse microdialysis which triggered localized changes in extracellular glutamate concentrations via NMDA infusion. In the cortex glutamate and γ- aminobutyric acid (GABA) are the principal neurotransmitters that mediate excitatory and inhibitory synaptic events respectively. Both have been extensively investigated by microdialysis in the rodent brain (Drew et al., 2004) NMDA has been shown to induce extracellular glutamate release *in vivo* in rat brain, using microdialysis (Young and Bradford, 1991). NMDA receptor activation has also been shown to facilitate the release of neurotransmitter from synaptosomes prepared from terminals in the hippocampus and neocortices (Sherman et al., 1991). The change in extracellular glutamate concentration evoked by reverse microdialysis was quantified using microdialysis and high-performance liquid chromatography (HPLC). qEEG was combined with the microdialysis to confirm the distinct impact associated with activation of surround inhibition versus glutamatergic excitation at motor cortex and hippocampus, respectively (Figure 1b). Concurrently, the contrasting electrophysiological results were quantified and confirmed with transcranial PA neuroimaging and qEEG recording (Figure 1c). Each modality thus provides useful information in different dimensions of specificity: spatial and temporal specificity from PA imaging, temporal specificity from qEEG, and focal neurochemical specificity from microdialysis in target neural circuits, i.e., motor cortex and hippocampus.

2 Material and Methods

Animal preparation. For the proposed *in vivo* experiments, 8-9-week-old male Sprague Dawley rats (Charles Rivers Laboratory, Inc., MA, United States) weighing 275-390g were used. The use of animals for the proposed experimental protocol was approved by the Institutional Animal Care and Use Committee of Johns Hopkins Medical Institute (RA16M225). Rats were housed in groups of 3 per cage with free access to food and water, and maintained on a 12hr light / 12hr dark cycle.

Fluorescence quenching-based near-infrared voltage-sensitive dye. In the present *in vivo* study, we used the fluorescence quenching-based near-infrared cyanine VSD, IR780 perchlorate (576409, Sigma-Aldrich Co. LLC, MO, United States) as in our previous *in vivo* study differentiating a chemoconvulsant seizure activity (Kang et al., 2017), and it have the analogous chemical structure of PAVSD800-2, our new VSD validated in our previous *in vitro* study.(Zhang et al., 2017) This VSD yields fluorescence emission leading to a reciprocal PA contrast with non-radiative relaxation of absorbed energy.

Microdialysis. On the day of the study the rats were weighed and anesthetized with urethane (1.2mg/kg,). Urethane was given incrementally with alternating ip and sc dosing. Three (3) ml of isotonic saline was given sc on each side of the body to keep the animal hydrated during the experimental procedure. Body temperature was maintained until animal was fully anesthetized and ready for surgery. For PA and EEG studies, an iv catheter was inserted into a tail vein prior to surgery for dye administration during the studies. Once a stable plane of anesthesia was established, hair was shaved from the scalp of each rat for improved optical/acoustic coupling for transcranial PA recording. The rat was placed into a stereotaxic device (Stoeling Co. Wood Dale, IL). This fixation procedure was required to prevent any unpredictable movement during PA or EEG recording of neural activities. A CMA12 microdialysis probe (Harvard Apparatus, Holliston, MA, USA) was implanted into either the right lobe of the frontal cortex (stereotaxic coordinates: 1.5 mm lateral and 3.2 mm anterior to bregma, and 3 mm below the surface of the dura) or the CA_3 region of the right hippocampus (stereotaxic coordinates: 3 mm lateral and 3.8 mm posterior to bregma, and 3.6 mm below the surface of the dura) (Paxinos and Watson, 2014). The probe active exchange surface was 2 × 0.5 mm. For EEG and PA experiments, probes were secured to the skull using dental acrylic cement.

***In vivo* microdialysis**. *In vivo* microdialysis sampling was carried out as previously described (Baumann et al., 2012; Elmore et al., 2017). For infusion experiments, NMDA (Sigma-Aldrich Chemicals, St. Louis, Mo) was weighed, solubilized, and diluted to the desired concentration in artificial cerebrospinal fluid (NaCl, 147 mmol/L; KCl, 2.7 mmol/L; $CaCl_2$, 1.2 mmol/L; $MgCl_2$, 0.85 mmol/L)(Harvard Apparatus, Holliston, MA, USA) on the study day. Once the probe was inserted and secured, it was perfused with artificial cerebrospinal fluid pumped at a flow rate of 2 µl/min. Samples were collected at 20 min intervals, and immediately transferred to a -80 °C freezer until assayed. To allow sufficient time for the glutamate levels to equilibrate, three baseline samples were collected an hour following initiation of infusion. Following these samples, NMDA was infused into the brain directly through the dialysis probe with the same pump parameters as used for the baseline samples. Dialysate samples were assayed for glutamate by a two-step process using HPLC-ECD on an Eicom HTEC-500 system (EICOM, San Diego, CA, USA). After passing the samples through a separation column, they were processed via a column containing immobilized L-glutamate oxidase enzyme, resulting in the release of hydrogen peroxide. The hydrogen peroxide concentration was then determined using a platinum working electrode. Chromatographic data were acquired online and exported to an Envision software system (EICOM, San Diego, CA, USA) for peak amplification, integration, and analysis.

200 **Quantitative EEG.** All EEG recordings utilized a three-electrode paradigm: 1 recording, 1 reference
201 (aligned to the site of activation) and 1 ground over the rostrum. The electrodes (IVES EEG; Model #
202 SWE-L25 – IVES EEG solutions, MA, USA) were fixed with minimal cyanoacrylate adhesive
203 (KrazyGlue), similar to previous protocols (Airan et al., 2017). Data acquisition was performed using
204 Sirenia software (Pinnacle Technologies Inc., Kansas, USA) with synchronous video capture. Data
205 acquisition had a 14-bit resolution, 400Hz sampling rate, and a band pass filter between 0.5 Hz and 60
206 Hz. The acquisition files were stored in an .EDF format and scored manually, using real time annotations
207 from the experiments. EEG power for 2-second epochs was done using an automated fast Fourier
208 transformation module in Sirenia software (Kang et al., 2018).

209 **Photoacoustic imaging.** We used real-time PA data acquisition to record electrophysiological neural
210 activities *in vivo*: an ultrasound research system consisted of an ultrasound linear array transducer (L14-
211 5/38) connected to a real-time data acquisition system (SonixDAQ, Ultrasonix Medical Corp., Canada).
212 The center frequency of the transducer was 7.1 MHz to obtain good sensing depth for neural activities in
213 deep brain tissue. To induce the PA signals, pulsed laser light was generated by a second-harmonic (532
214 nm) Nd:YAG laser pumping an optical parametric oscillator (OPO) system (Phocus Inline, Opotek Inc.,
215 USA), providing 690-900 nm of tunable wavelength range and 20 Hz of the maximum pulse repetition
216 frequency. A bifurcated fiber optic bundle, each 40 mm long and 0.88 mm wide, was used for laser pulse
217 delivery. The PA probe was posed between the outlets of the bifurcated fiber optic bundles using a
218 customized, 3-D printed shell for evenly distributed laser energy density in the lateral direction on rat
219 scalp surface. The alignment of outlets was focused specifically at 20 mm depth. The PA probe was
220 positioned in the sagittal plane to cover the barrel cortex and hippocampus at the same time. Lateral
221 position of the probe was at the contra-lateral side of microdialysis probe: 1.5 mm for motor cortex
222 recording; 3 mm for hippocampus. The distance between the PA probe and the rat skin surface was 20
223 mm filled with acoustic gel, and the resultant energy density was at ~5 mJ/cm^2 , which is far below the
224 maximum permissible exposure (MPE) of skin to laser radiation by the ANSI safety standards. (Anon,
225 1975) A wavelength of 790 nm was used, at which sufficient absorbance can be obtained by the near-
226 infrared VSD, i.e., IR780 perchlorate. Also, probing at the wavelength prevented the undesired time-
227 variant change of oxygen saturation, being at the isosbestic point of Hb and HbO_2 absorption spectra.
228 Fig. 4b presents a representative sagittal cross-sectional PA image of a rat brain. The brain outline was
229 drawn based on the rat brain atlas (Paxinos and Watson, 2014).

230 ***In vivo* experimental protocol.** The *in vivo* protocols were designed for simultaneous multi-modal
231 sensing of the neural activity at motor cortex and hippocampus: microdialysis-qEEG and microdialysis-
232 PA imaging. Figure 2 shows a detailed schematic protocol for each group representing the response to
233 the administration of NMDA, Lexiscan and VSD (i.e., IR780 perchlorate). PA and qEEG data
234 acquisition was performed for 40 min to correlate with three microdialysis samples collected at 20-min
235 intervals. VSD and Lexiscan followed the data acquisition sequence with 3-min delay, thereby 5 min of
236 baseline phase was guaranteed for neural activity index reconstruction in PA imaging before starting
237 NMDA infusion. The dosing protocol for Lexiscan and VSD administration was as follows: through an
238 iv tail vein catheter, 150 μl of Lexiscan (0.4mg/5ml) was injected, followed by 200 μl of VSD at 2mg/ml
239 concentration, flushed immediately with 150 μl of 0.9% isotonic saline. The EEG signal at motor cortex
240 was recorded an identical preparation procedure as the PA imaging, including animal preparation and
241 administration of IR780, Lexiscan and experimental duration time for all recordings.

242 **Brain histology.** Rats used for the above protocol were sacrificed, and whole brains immediately
243 harvested and placed in 10% formalin. All brains were allowed to fix in fresh 10% formalin for at least
244 48 hours with gentle agitation on a conical rotator. Subsequently, the brains were processed through a
245 series of sucrose gradients (15%, 20%, 30% for 12-24 hours each) for cryoprotection. Brains were
246 sectioned frozen at 300 μm thickness. Tissue sections were mounted on slides in ProLong Diamond

247 Anti-face mountant. Slides with sections were imaged using an Olympus OM-D E-M5 Mark II for bright
248 field image and using LI-COR Odyssey for fluorescence visualization.

249

250 **3 Results**

251 **NMDA-evoked glutamatergic neurotransmission.** Figure 3 shows the effect of NMDA infusion on
252 glutamate release in the motor cortex and the hippocampus of anesthetized rats. Concentrations of
253 glutamate in the dialysate were calculated from values of three baseline samples collected at 20
254 minutes intervals before NMDA infusion. NMDA was diluted into artificial cerebrospinal fluid at the
255 required concentration, and infused into the brain through the microdialysis probe. During infusion,
256 samples continued to be collected every 20 minutes for the remainder of the study. Figure 3a shows that
257 infusion of 0.3 mM NMDA into the motor cortex caused a roughly 60 % increase in glutamate levels as
258 compared to baseline samples. The increase occurs in the first 20-minute sample collection
259 period following the beginning of the NMDA infusion, and is sustained for the full infusion period.
260 Figure 3b demonstrates the effects of infusion of 0.3, 1.0, and 3.0 mM NMDA into the hippocampus.
261 0.3 mM NMDA appears to cause a roughly 40 % increase in glutamate levels, that remains for the
262 duration of the infusion; the 1.0-mM NMDA infusion appears to cause approximately double the
263 glutamate levels in the hippocampus compared to baseline. This increase provoked by the dose
264 is also sustained until the termination of the NMDA infusion. However, at 3.0-mM NMDA infusion a
265 roughly 6-fold increase in glutamate levels was observed when compared to baseline values. This increase
266 peaks during the second 20-minute sample period and start a steady declined before the infusion period
267 is completed. The increase in glutamate release seen in both the motor cortex and the hippocampus
268 appear to be validated by VSD imaging in the PA. In contrast the EEG recording showed no seizure
269 activity with the motor cortex infusion at the concentration used, but elicited a strong seizure response in
270 the hippocampus with 3mM NMDA within the same timeframe as peak glutamate activity in the
271 dialysate.

272 **EEG of electrophysiological activity in motor cortex and hippocampus.** We used qEEG to validate
273 for the NMDA-induced activation of the circuits in motor cortex vs. hippocampus to establish circuit
274 activity differences to the focal stimulation protocol. These qEEGs allowed for the interpretation of the
275 PA experiment data acquired using the same protocols to help access spatial and temporal specificities.
276 The temporal specificity of EEG allowed for the evaluation of circuit responses in real time, before and
277 after focal NMDA infusion. EEG lacks spatial resolution, and is not able to record from deep brain
278 structures using leads placed on the brain or skull surface. We did not opt to put in depth electrodes to
279 keep the experiments as non-invasive as possible. The stimulation had to be focal since we have already
280 shown the proof of concept that PA can detect onset of generalized seizure through an intact skull
281 (Kang et al., 2017). Therefore, we used a microdialysis probe to deliver 0.3 - 3 mM NMDA to distinct
282 motor cortex and hippocampal circuits (Figure 1a) (Paxinos and Watson, 2014). The results show that an
283 NMDA infusion of 0.3 mM NMDA in the M2 coordinates of the motor cortex caused an expected rise
284 in local glutamate concentration (Figure 3) which however had a paradoxical effect on the EEG spectral
285 power, specifically in the gamma frequency (Figure 4-a2). The EEG suppression indicated a focal
286 glutamate-induced activation of surround-inhibition, which became more prominent over the duration of
287 the infusion (Figure 4-b2). In contrast, a 3 mM infusion into the hippocampus resulted in an immediate
288 increase in bursts of gamma power in the EEG followed by a focal seizure (Figure 4 and S1). Unlike the
289 cortical circuit that showed increasing EEG suppression over time, the hippocampal circuit continued to
290 exhibit short epileptiform discharges throughout the NMDA infusion period (Figure S1b V) indicating
291 continued disruption of the DG 'gating' during the entire duration of the NMDA infusion.

292

Transcranial PA imaging. Figure 5 shows the transcranial PA neuroimaging of distinct neural mechanism at motor cortex and hippocampus. The sagittal PA imaging plane was selected in the contralateral side of the microdialysis probe infusing NMDA into the brain – motor cortex and hippocampus were recorded at 1.5 mm and 3 mm of lateral positions, respectively (Figure 5a). Figure 5b present the sagittal PA cross-sections, and white dotted rectangular indicators are the regions for temporal-frequency analysis reconstruction proposed in our previous literature to augment VSD responses of neural activities. Dotted line indicates the boundary of sagittal section derived from the rat brain atlas and scaled accordingly(Paxinos and Watson, 2014). The solid line represents the region-of-interest for neural activity map reconstructions. Detailed information of neural activity reconstruction can be found in our previous publication (Kang et al., 2017). From the time-sequence of PA image, the normalized neural activity index of each neural circuitry was presented as a function of normalized PA intensity. Note that the reference intensity was obtained from the baseline phase: 5-10 min (Figure 5c). At motor cortex, 0.3-mM NMDA infusion presented complex suppression mechanism in the cortical region: The quantification of normalized neural activity index presented 1.00 ± 0.36, 0.87 ± 0.37, and 1.19 ± 0.36 for baseline (5 – 10 min), and first (10 – 30 min) and second (30 – 40 min) NMDA infusion phases (NMDA1 and NMDA2), respectively. This result suggests the initial suppression at the first 20 min of NMDA infusion (i.e., -13 %), and following recovery above the basal level, which is well correlated to the electrophysiological validation in qEEG recording (Figure 4-a2). On the other hand, 3-mM NMDA infusion at hippocampus yielded significant elevation of neural activity index as corresponding PA intensity decreases, which validates the proposed VSD mechanism which is suppressive to neuronal depolarization (Zhang et al., 2017): 1.00 ± 0.35 %, 1.55 ± 0.36 %, and 1.74 ± 0.33 % of normalized neural activity indices for baseline, NMDA1, and NMDA2 phases, respectively. Otherwise, focal 0.3 mM NMDA infusion at hippocampus did not presented any statistical significance compared to the baseline neural activity index: 1.00 ± 0.31 %, 0.99 ± 0.41 %, and 0.76 ± 0.34 % of normalized neural activity indices for baseline, NMDA1, and NMDA2 phases, respectively. These results support our hypothesis that PA imaging can differentiate the DG gating function at the hippocampus. In all, the 3-mM NMDA infusion at hippocampus presented statistically significant difference compared to those with 0.3 mM at both hippocampus and motor cortex ($P < 0.0001$). The VSD mechanism suppressive to neuronal depolarization could be also confirmed with the temporal specificity of PA neuroimaging. Figure 5d presents the normalized neural activity index and relative PA intensity to baseband frequency component. As shown in the figure, NMDA inset produces suppressive PA intensity around 1-dB, , which is also synchronized to the huge discharge presented in qEEG given by DG gating breakdown (Figure 4-b2), leading to 2.5-times instantaneous increase of neural activity index for around 20 sec. Refer Figure S2 for the entire neural activity index and PA intensity traces.

Figure 6 presents the normalized neural activity index as a function of extracellular glutamate concentration at motor cortex and hippocampus. The motor cortex presents the comparable amount of neural activity index with that of baseline phase at hippocampus (n = 1), but 3 mM NMDA infusion into hippocampus produced exponential increase in neural activity index when the extracellular glutamate concentration exceeds 6 μM in microdialysis sampling (n = 2). These results again confirm the DG breakdown with specific glutamatergic potential threshold at neural circuitry.

Brain histology. Brain tissue was extracted after all *in vivo* experimental protocols. The brain was frozen-sectioned *into* 300-μm thickness slices and evaluated to confirm probe placement using the hemorrhage caused by the microdialysis probe insertion for the NMDA infusion and collection of extracellular fluid sampling used for glutamate quantification. Figure 6 shows the bright-field images of the coronal plane of the motor cortex and hippocampus at 3.2 mm and -3.8 mm from bregma, respectively. White arrows indicate the hemorrhage caused by the microdialysis probe positioned at the following coordinates: bregma 3.2 mm, lateral 1.5 mm, depth 2.5 mm for motor cortex; bregma -3.8 mm, lateral 3 mm, and depth 3.6 mm for hippocampus. The VSD staining of brain tissue was confirmed with near-infrared

fluorescence microscopy. Uniform VSD fluorescence was found in the VSD perfusion group, while negative control (VSD -) presented negligible fluorescence emission (Figure S3), which confirms the results in our previous publication (Kang et al., 2017).

4 Discussion

The set of experiments described here yield key findings as follows: (1) The microdialysis-dependent NMDA infusion into the central nervous system (CNS) lead to a reliable increase in focal extracellular glutamate concentrations in both the cortex and hippocampus. (2) Unlike the microdialysis glutamate release for both cortex and hippocampus, transcranial PA imaging and qEEG showed distinct phenotypes in the cortex vs. hippocampus. There was a fall in electrophysiological responses in the motor cortex indicating NMDA receptor activation in the motor cortex circuit lead to strong activation of surround inhibition (Sachdev et al., 2012). In contrast, NMDA activation in the hippocampus triggers an all-or-none type of circuit dynamics that lead to the initiation of a focal seizure in the hippocampal circuit. (3) Transcranial PA neuroimaging data successfully validated these EEG specific opposite circuit activity profiles for the similar focal activation of NMDA receptors. No circuit activity was detected in the motor cortex on the PA imaging despite an increase in focal glutamate levels recorded in the same rats. In contrast, the PA signal yielded hot spots of neuronal activity following NMDA receptor activation in the hippocampus.

These results allow us to reassess the differential neural mechanisms modulating activity between motor cortex and hippocampus as described in the Introduction: Strong surround inhibition has been observed with transcranial PA neuroimaging and qEEG recording. Cortical inhibition may be due to suppression of neuronal firing mediated by γ-amino butyric acid (GABA) receptors (Krnjević, 1997) secondary to activation of GABAergic inhibitory interneurons by NMDA (Homayoun and Moghaddam, 2007). Slice electrophysiology in animal and human cortical tissue have revealed two main phases of inhibition following stimulation; a "fast" phase mediated by ionotropic $GABA_A$ receptors and a "slow" phase mediated by metabotropic $GABA_B$ receptors (Connors et al., 1988; McCormick, 1989). In the CNS, one physiological mechanism to select neuronal responses and to focus neural activity is surround inhibition or lateral inhibition (Beck and Hallett, 2011). Inhibition provides differentiation of neural activity, which is critical for proper sensorimotor inputs and outputs. A similar phenomenon of surround or lateral inhibition was observed on the cortical level in models of focal epilepsy, in which autoradiography with [^{14}C]deoxyglucose was used to study the architectural pattern of glucose utilization in the motor cortex of rats during focal penicillin seizures (Collins and Mehta, 1978). Results from this study showed that besides the 2-or 3-fold increase of glucose metabolism in the center of the epileptic focus, in cortex surrounding the epileptic focus there was an increase in synaptic inhibition resulting in a normal or slight decrease in autoradiographic density (Collins and Mehta, 1978). Such findings likely indicate a general pattern of cellular connectivity intrinsic to cortical organization.

On the other hand, the hippocampal circuitry provides a second distinct circuit that contrasts with that of the motor cortex to assess PA specificity, as it reveals the proportional excitation of glutamatergic neurotransmission. The DG of the hippocampus is positioned as a gatekeeper for the canonical trisynaptic circuit, regulating the vast cortical inputs that regulate the limbic system. Characteristically, the DG displays a high activation thresholdd; a trait that is associated with executing cognitive functions that require pattern separation and completion (Chawla et al., 2005). The ability to differentiate inputs, and diversify cognitive functions, is mediated by inhibition. Suitably, the DG is profusely innervated with strong GABAergic inhibition (Szabo et al., 2017). In diseases of hyperexcitability, such as epilepsy, the DG can regulate pathological seizure activity from invading the

386 limbic system. This gating is evident in recordings from the DG during low frequency stimulation of the
387 perforant path fibers. The DG displays the ability to selectively filter low frequency stimulation by
388 subsequent activation of strong inhibitory post synaptic potentials (Andersen et al., 1966). Yet, longer or
389 higher frequency stimulations resulted in excitatory post synaptic potentials generated by the DG. This
390 disruption of DG gating has been clearly demonstrated by utilizing VSD imaging techniques, reinforcing
391 DG's role of gatekeeping (Ang et al., 2006). The consequence of gatekeeping is that in epilepsy the DG
392 generates and propagates seizure activity.

393 Further investigations are required to advance our current perspectives available with tri-modal
394 sensing, including PA, qEEG, and microdialysis. Previous studies have shown that application of
395 glutamate to the hippocampal pyramidal neurons produces a fast-rising brief depolarization (Taube and
396 Schwartzkroin, 1987). Therefore, the use of PA will enable us to more precisely assess glutamate and
397 GABA dynamics in order to formulate a more complete profile of circuit activation. Once homeostasis is
398 disrupted, neuronal activity is sensitive to changes both of excitatory and inhibitory mechanisms. . Faster
399 neurochemical recording is another approach that may prove useful in assessing the impact of these
400 measures. Although microdialysis successfully provided quantitative, focal neurochemical
401 concentrations, the sampling rate of 1 sample per 20 min was slow. Techniques offering faster temporal
402 resolution may allow more meaningful comparison of the neurochemical changes yielded by
403 microdialysis and the electrophysiological events monitored by qEEG and PA imaging. One such
404 technique, using custom built hardware and the Amplex Red method, achieved fluorescence-based
405 quantification of glutamate from samples taken every 5 seconds, though reliability appeared to be limited
406 when higher glutamate concentrations were measured (Medina-Ceja et al., 2015). Implantable glutamate
407 biosensors allow sub-second readouts of neurochemical concentrations. However, current limitations
408 include sensitivity, selectivity, and high cost; recent developments in materials, effective modeling, and
409 sensor design may soon alleviate some of these limitations (Clay and Monbouquette, 2018; Moon et al.,
410 2018).

411 EEG records the voltage differentials occurring between the reference and recording electrode
412 representing underlying circuit activity with high temporal specificity. Hypersynchronous neuronal
413 activity in any given circuit results in high amplitude high frequency activity in the EEG, causing the
414 generation of very large-amplitude excitatory post-synaptic potentials. In contrast, interneurons known
415 to fire action potentials at very high frequencies inhibit neuronal circuit activity efficiently because a
416 single interneuron can innervate and inhibit a large population of pyramidal neurons simultaneously.
417 Depending on the circuit, simultaneous interneuron activation can be followed by a rebound
418 depolarization due to simultaneous disinhibition of the excitatory neurons innervated by this interneuron
419 population.

420 Based on the validated circuit activity measured via transcranial PA imaging and qEEG
421 successfully differentiated the circuit activity between these regions with spatial and temporal specificity.
422 However, future developments should serve to further advance the efficacy of PA imaging in
423 neuroscience. (1) we expect that improved signal processing for extracting neural activity from the
424 ubiquitous blood context will enable better characterization of brain function. The present in vivo
425 experiments confirmed the possibility of background suppression. Enhanced signal processing and/or
426 use of multi-spectral wavelengths may allow significantly improved spectral differentiation of
427 electrophysiological activities in the brain, leading to development of novel quantitative metrics for real-
428 time brain activity measures. Having isotropic resolution with 2-D PA probe would be also an interesting
429 direction to pursue as follow up to the present work. The use of 2-D PA probe would not only allow
430 real-time volumetric information, but also enable the suppression of off-axis interference. Even though
431 we presented that neural activity can be successfully discerned with current 1-D PA probe, its sensitivity
432 might be affected by off-axis interferences especially from the elevation direction because of the limited

acoustic lens focusing at a fixed depth. The neuroimaging using 2-D PA probe would reject those interferences by the advanced electrical beamforming capability in axial, lateral, and elevation directions.

In all, the EEG results indicate that NMDA infusion and the associated increase in focal glutamate had opposite physiological results in the two circuits: NMDA triggers glutamate release that excites the neural circuit, but it is nearly immediately blocked by surround inhibition at motor cortex or causes runaway excitation in the hippocampus by overcoming DG gating. This is reflected in the lower seizure threshold of the hippocampus compared to neocortex. This suggests that the activations of NMDA receptors can modulate neural circuits into diametrically opposite responses *in vivo*. Transcranial PA imaging demonstrated its ability to differentiate the changes in electrophysiology found in these circuits, and its findings were validated with qEEG. PA imaging is a promising technology for the imaging of neural events in real time.

5 Author Contributions

AAG, DFW, SDK, EMB and LML originally conceived of the presented idea and helped to design the overall research plan, and also MB helped plan specific experiments and all contributed to the review and writing of the manuscript. JK, SDK, JSE, BJS, HV planned and carried out *in vivo* experiments, analyzed the research outcomes, and wrote the first draft of the manuscript. APM performed histopathological analysis. AR, MB, AG also contributed to the final version of the manuscript. All authors provided critical feedback and helped shape the research, analysis and manuscript.

6 Acknowledgments

This work was supported by the NIH Brain Initiative under Grant No. R24MH106083-03 and the NIH National Institute of Biomedical Imaging and Bioengineering under Grant No. R01EB01963. NIH National Institute of Child Health and Human Development (NICHD) for R01HD090884 (S. D. K.).

7 Conflict of Interest Statement

The authors declare that the research was conducted in the absence of any commercial or financial relationships that could be construed as a potential conflict of interest.

460 **Figures**

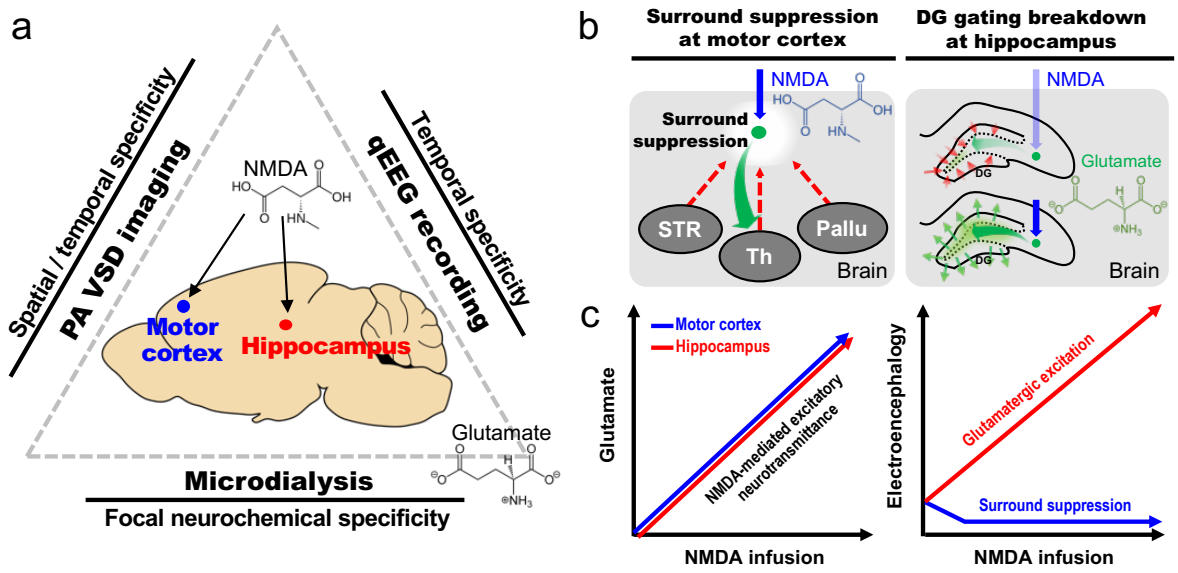

461

462 **Figure 1 Tri-modal sensing of distinct changes in electrophysiology at motor cortex and hippocampus.**
463 (**a**) Tri-modal neural sensing approach. (**b**) surround suppression at motor cortex and dentate gyrus (DG) gating
464 breakdown at hippocampus to a focal NMDA infusion. (**c**) Diversion of an electroencephalogy for NMDA-
465 mediated glutamatergic neurotransmissions. NMDA, N-methyl-d-aspartate; STR, subthalamic nucleus; Th,
466 Thalamus; Pallu, Pallidus.

467

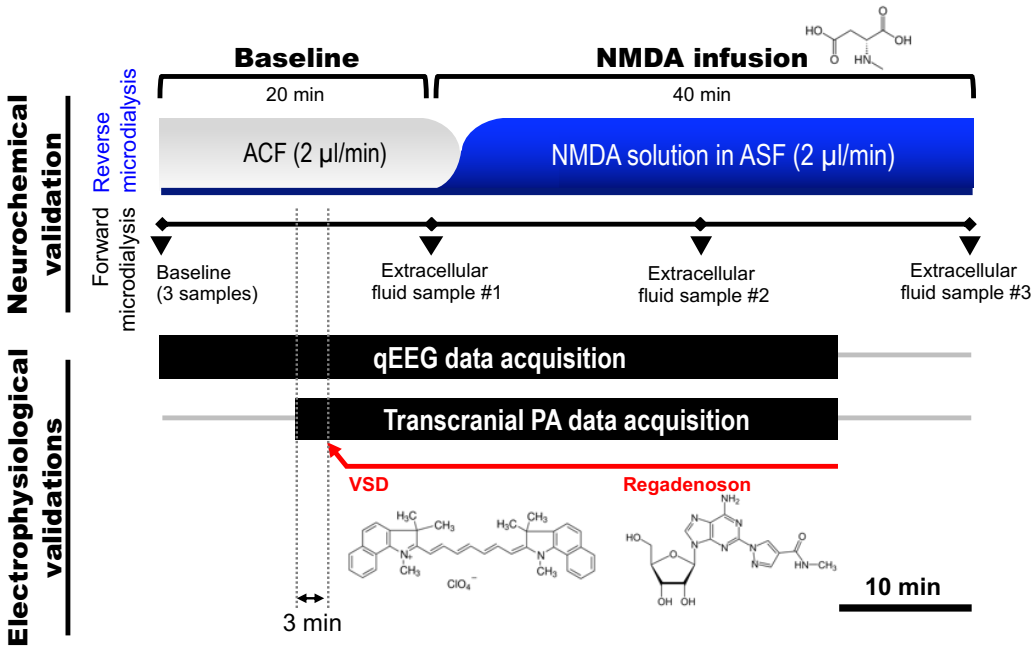

468

469 **Figure 2 *In vivo* experimental protocol.** Tri-modal sensing of distinct mechanisms at motor cortex and
470 hippocampus using forward microdialysis, PA imaging, and qEEG. ACF, artificial cerebrospinal fluid.

471

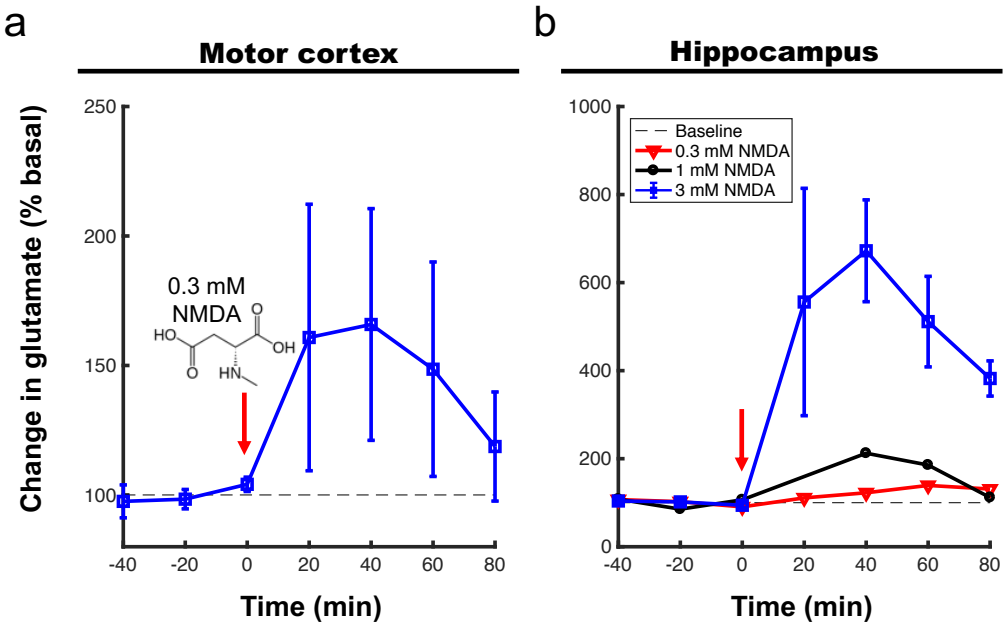

472

473 **Figure 3. The effects of NMDA infusion on extraceullular glutamate concentrations in anesthetized rats,**
474 **as compared to % baseline.** (**a**) 0.3 mM NMDA infusion into the motor cortex causes the glutamate to increase,
475 culminating in a 65% increase as compared to % baseline. (**b**) 0.3, 1.0, and 3.0 mM NMDA infusion into the
476 hippocampus caused maximal glutamate increases of 39%, 112%, and 572% respectively as compared to %
477 baseline.

478

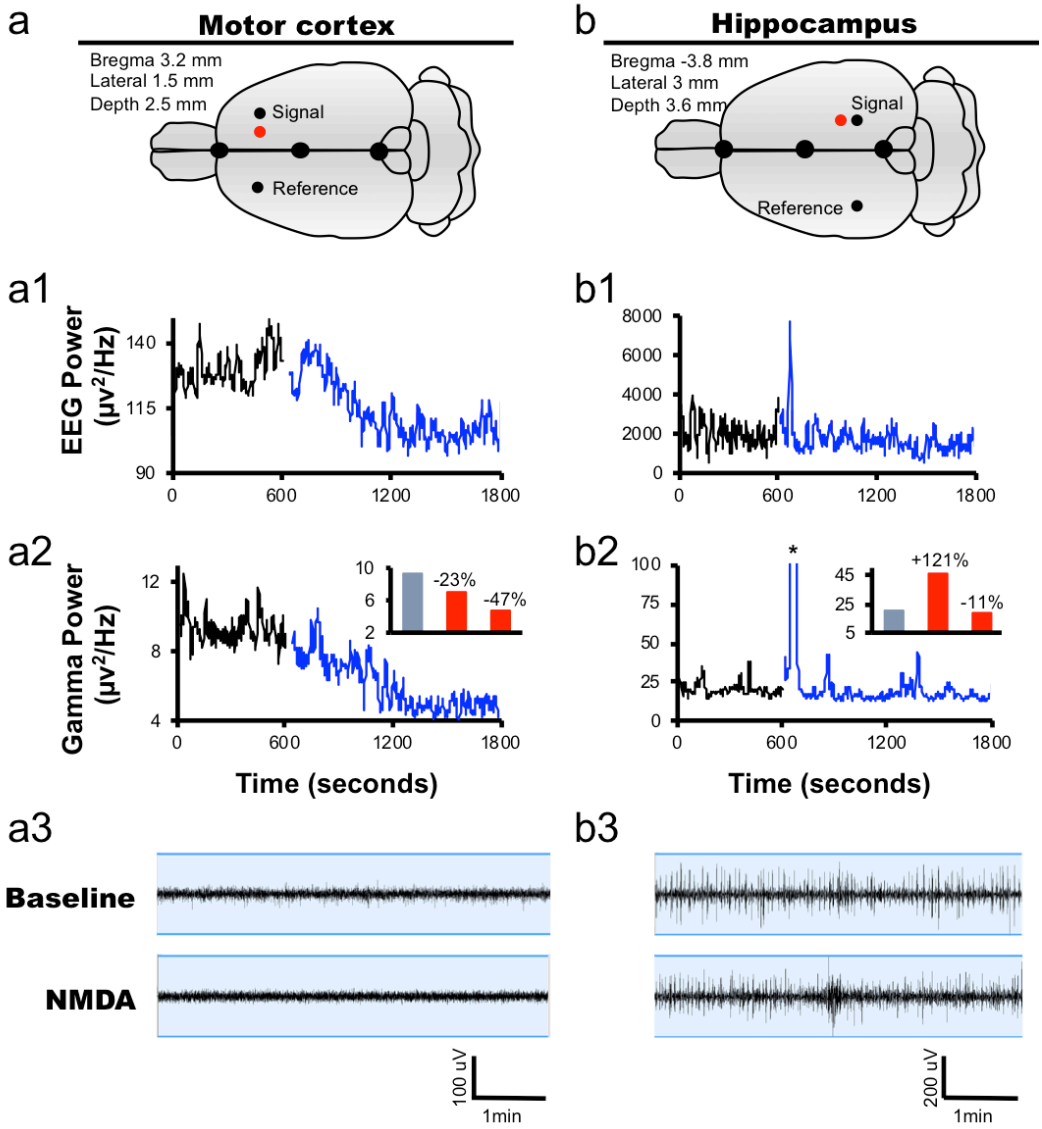

Figure 4. qEEG of motor cortex and hippocampus circuit dynamics following focal NMDA infusion. (**a**) Illustrates stereotaxic coordinates for the microdialysis probe and recording leads for the motor cortex. Ground electrode was implanted over the rostrum for both locations. Full EEG power (**a1**) shows a 10-minute baseline recording (blue trace), followed by two consecutive 10 min traces (red traces) of focal NMDA infusion. Overall EEG showed a drop in power after onset of focal NMDA infusion. (**a2**) Respective gamma power with baseline (blue trace) and focal NMDA infusion (red trace); power drop in gamma over the NMDA infusion period (first 10-minutes 23% decrease, second 10-minute 47% decrease when compared to baseline; see inset). (**a3**) Five minute raw EEG traces, blue lines indicate +/- 200uV, (attenuation of EEG waveforms seen with NMDA). (**b**) Illustrates stereotaxic coordinates for the microdialysis probe and recording leads for the hippocampus. Full EEG power (**b1**) shows a 10-minute baseline recording (blue trace), followed by two consecutive 10 min traces (red) of focal NMDA infusion. In contrast to the motor cortex, hippocampal EEG demonstrated onset of epileptiform discharges. (**b2**) Respective gamma power trace for hippocampal recordings demonstrates a 121% increase in gamma in the first ten minutes, and an 11% decrease in the second ten minutes, when compared to baseline (see inset). (**b3**) Five-minute raw EEG traces of the hippocampus, blue lines indicate +/- 200uV, NMDA infusion increased epileptiform activity, seizure indicated by asterisk in b2. For expanded time scales of hippocampal seizure see Supplemental 1.

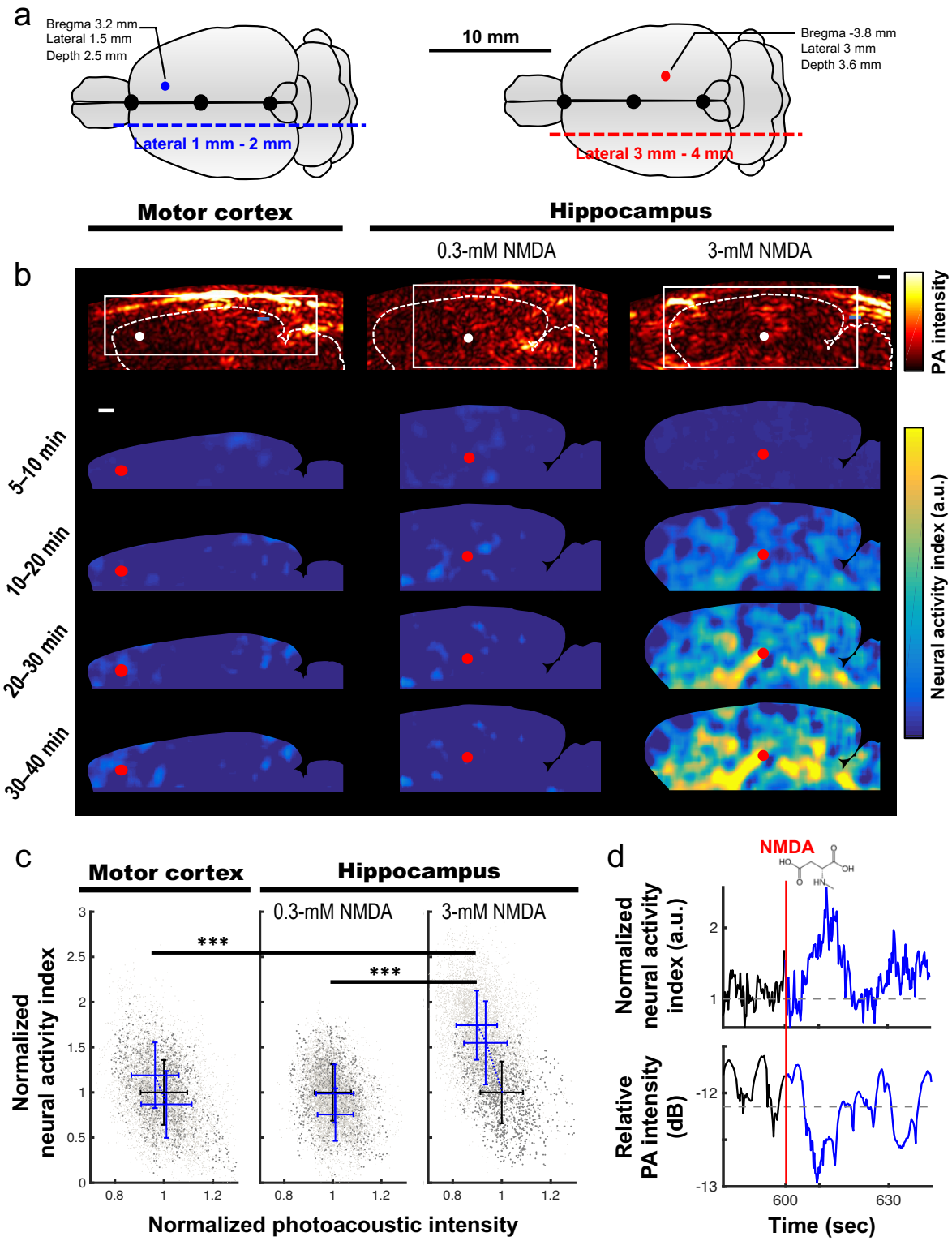

Figure 5. Transcranial PA neuroimaging of the distinct circuit dynamics at motor cortex and hippocampus following focal NMDA infusion. (**a**) Illustration of stereotaxic coordinates for the microdialysis probe and sagittal cross-sections for real-time PA recording. (**b**) Sagittal PA cross-sections

502 at 790 nm and time-averaged neural activity maps at each time points: 5-10 min; 10-20 min; 20-30 min;
503 30-40 min. Note that white and red points in (b) indicate microdialysis probe in contra-lateral positions.
504 (**c**) Normalized neural activity indices as a function of corresponding normalized PA intensities. Black
505 lines: baseline; blue lines: first and second NMDA infusion phases. Dotted blue line indicates the
506 progression of the correlation between the normalized neural activity indices and PA intensities. (**d**)
507 Instantaneous suppression of PA intensity at the onset of NMDA infusion, which also presented with
508 qEEG in Figure 4-b2, leading to the high-intensity neural activity index trace.

509

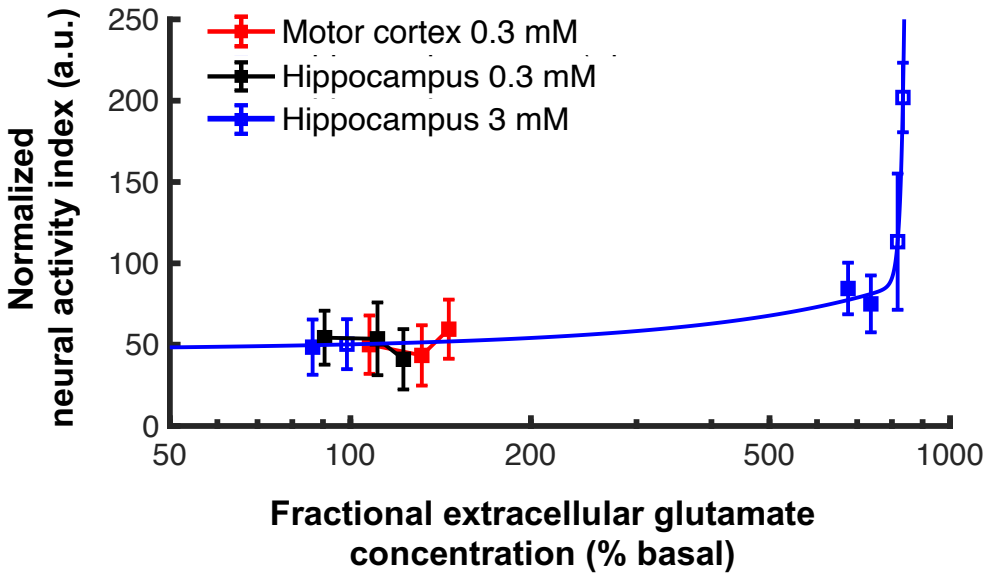

510

511 **Figure 6. Normalized neural activity index as a function of extracellular glutamate concentration at**
512 **motor cortex and hippocampus.**

513

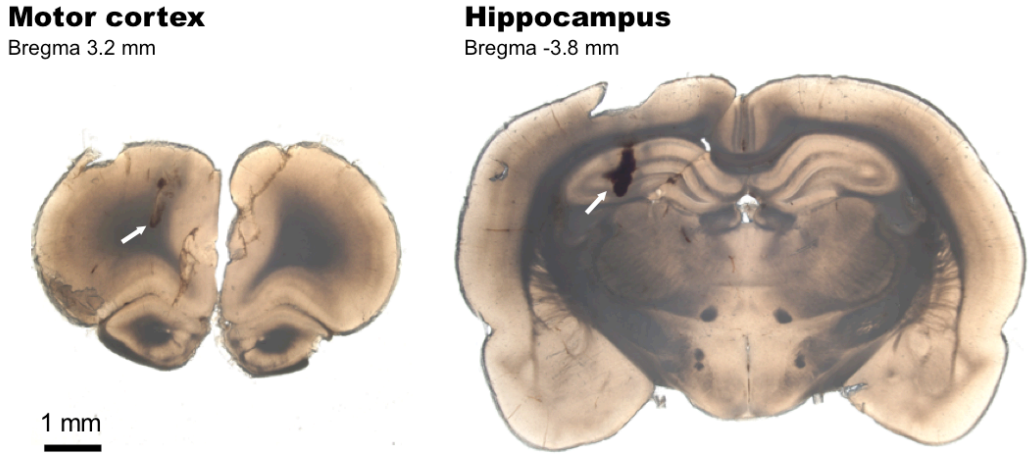

514

515 **Figure 7. Histopathological confirmation of microdialysis probe at motor cortex and hippocampus.** White
516 arrow indicates the wound caused by microdialysis probe installation.

517

518 **Supplementary Material**

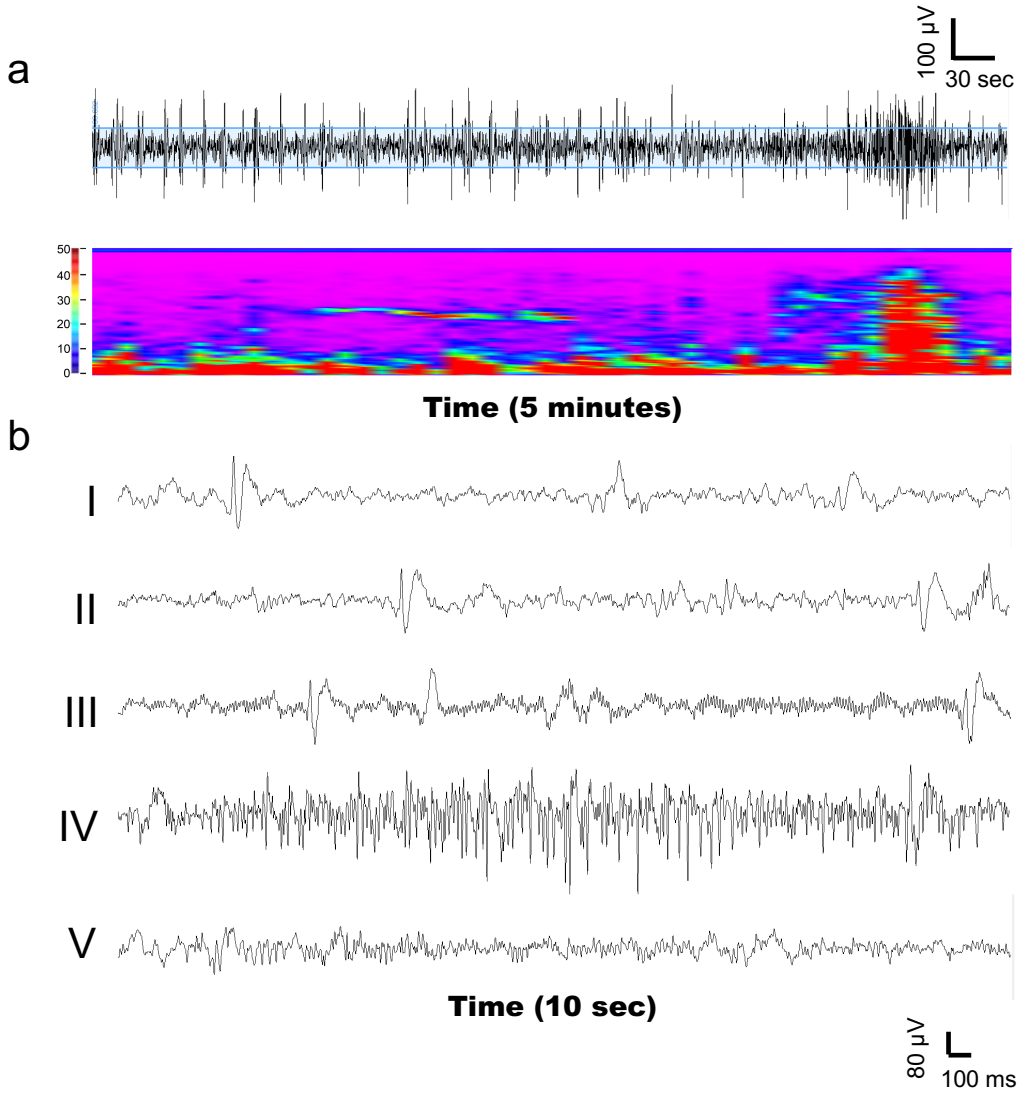

519

520 **Figure S1. Expanded time scale of EEG recording in the hippocampus.** (**a**) Raw trace (5 minutes) shows
521 ramping up of gamma power (see heatmap, 0-50Hz) before onset of focal seizure. (**b**) 10 second expanded time
522 scale of raw EEG traces from hippocampal EEG recording. (I) Baseline (II) immediately after onset of NMDA
523 infusion (III) ramping up of gamma power before seizure event (IV) focal seizure event (V) short duration high
524 frequency hippocampal discharges over the duration of the 20 minute recording (n=4 events within EEG
525 recording).

526

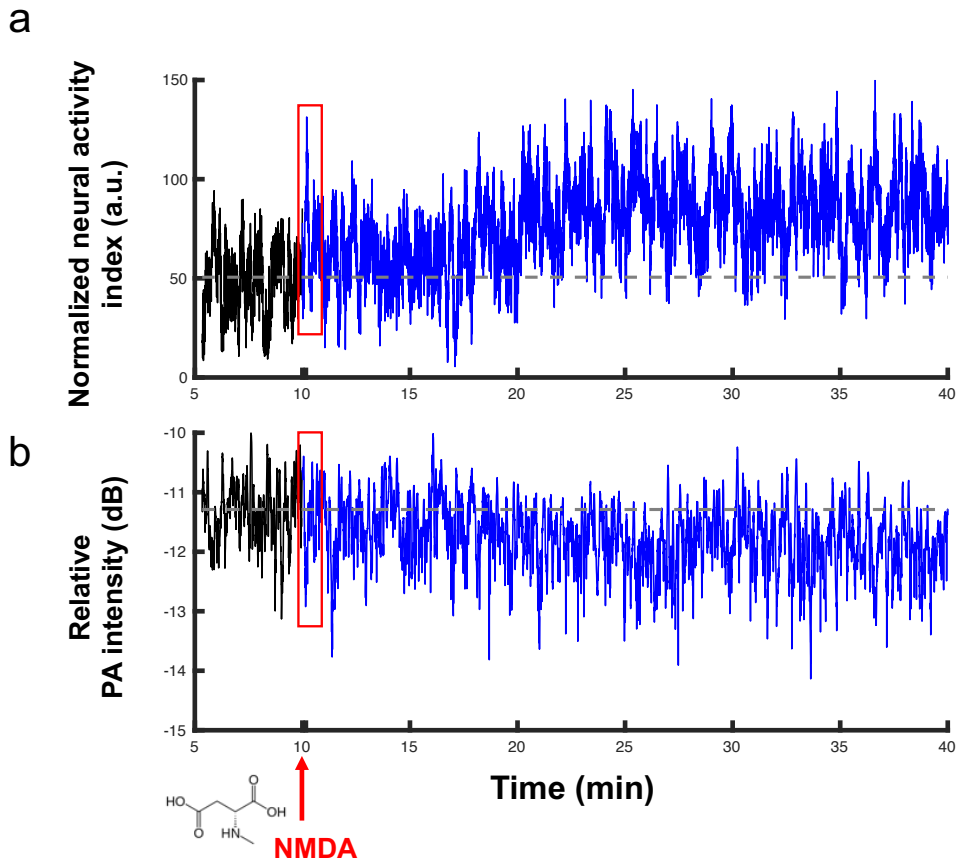

527

528 **Figure S2. PA quantification of a focal seizure with 3 mM NMDA infusion at hippocampus.** (**a**)
529 normalized neural activity index and (**b**) corresponding relative PA intensity traces. Red rectangular indicators
530 show the regions-of-interest used for Figure 5d.

531

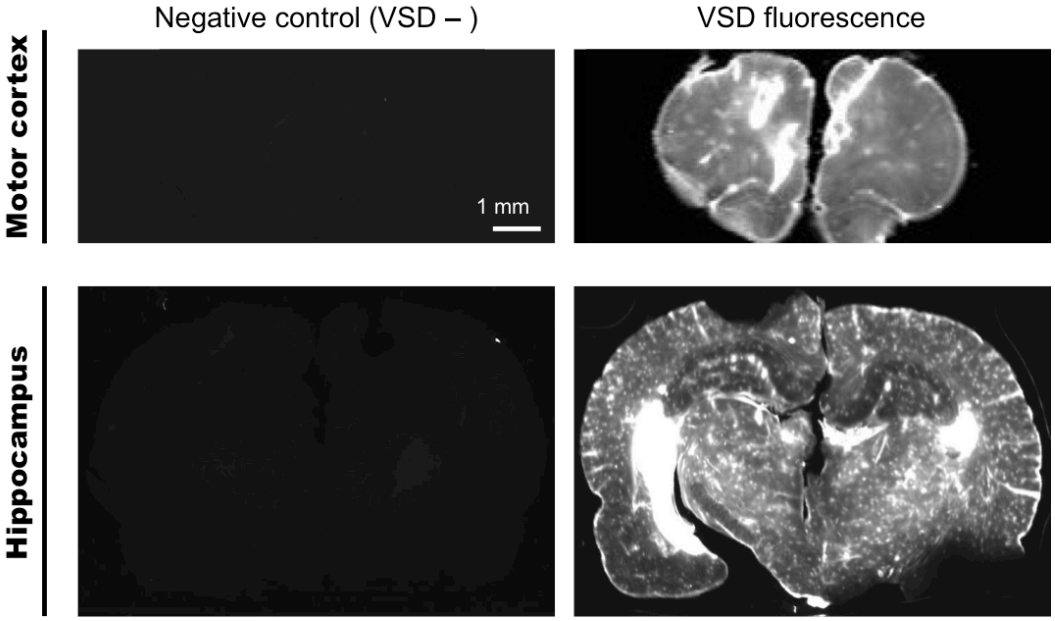

532

533 **Figure S3. Frozen-sectioning histopathological confirmation of systematic VSD delivery through BBB**
534 **using pharmacological modulation.**

535

536 **References**

537

538 Airan RD, Meyer RA, Ellens NPK, Rhodes KR, Farahani K, Pomper MG, Kadam SD, Green JJ (2017)
539 Noninvasive Targeted Transcranial Neuromodulation via Focused Ultrasound Gated Drug Release
540 from Nanoemulsions. Nano Lett 17:652–659.

541 Andersen P, Holmqvist B, Voorhoeve PE (1966) Entorhinal Activation of Dentate Granule Cells. Acta
542 Physiologica Scandinavica 66:448–460.

543 Ang CW, Carlson GC, Coulter DA (2006) Massive and specific dysregulation of direct cortical input to
544 the hippocampus in temporal lobe epilepsy. J Neurosci 26:11850–11856.

545 Anon (1975) American National Standard for the Safe Use of Lasers. Annals of Internal Medicine
546 82:132.

547 Baumann MH, Ayestas MA, Partilla JS, Sink JR, Shulgin AT, Daley PF, Brandt SD, Rothman RB, Ruoho
548 AE, Cozzi NV (2012) The designer methcathinone analogs, mephedrone and methylone, are
549 substrates for monoamine transporters in brain tissue. Neuropsychopharmacology 37:1192–1203.

550 Beck S, Hallett M (2011) Surround inhibition in the motor system. Exp Brain Res 210:165–172.

551 Chawla MK, Guzowski JF, Ramirez-Amaya V, Lipa P, Hoffman KL, Marriott LK, Worley PF,
552 McNaughton BL, Barnes CA (2005) Sparse, environmentally selective expression of Arc RNA in the
553 upper blade of the rodent fascia dentata by brief spatial experience. Hippocampus 15:579–586.

554 Clay M, Monbouquette HG (2018) A Detailed Model of Electroenzymatic Glutamate Biosensors To Aid
555 in Sensor Optimization and in Applications in Vivo. ACS Chem Neurosci 9:241–251.

556 Collins RC, Mehta S (1978) Effect of amino-oxyacetic acid (AOAA) on focal penicillin seizures. Brain
557 Res 157:311–320.

558 Connors BW, Malenka RC, Silva LR (1988) Two inhibitory postsynaptic potentials, and GABAA and
559 GABAB receptor-mediated responses in neocortex of rat and cat. The Journal of Physiology
560 406:443–468.

561 Crescenzi R, DeBrosse C, Nanga RPR, Byrne MD, Krishnamoorthy G, D'Aquilla K, Nath H, Morales
562 KH, Iba M, Hariharan H, Lee VMY, Detre JA, Reddy R (2017) Longitudinal imaging reveals
563 subhippocampal dynamics in glutamate levels associated with histopathologic events in a mouse
564 model of tauopathy and healthy mice. Hippocampus 27:285–302.

565 Deán-Ben XL, Sela G, Lauri A, Kneipp M, Ntziachristos V, Westmeyer GG, Shoham S, Razansky D
566 (2016) Functional optoacoustic neuro-tomography for scalable whole-brain monitoring of calcium
567 indicators. Light Sci Appl 5:e16201–e16207.

568 Derdikman D, Hildesheim R, Ahissar E, Arieli A, Grinvald A (2003) Imaging spatiotemporal dynamics
569 of surround inhibition in the barrels somatosensory cortex. J Neurosci 23:3100–3105.

570 Drew KL, Pehek EA, Rasley BT, Ma YL, Green TK (2004) Sampling glutamate and GABA with
571 microdialysis: suggestions on how to get the dialysis membrane closer to the synapse. J Neurosci
572 Methods 140:127–131.

573 Elmore JS, Dillon-Carter O, Partilla JS, Ellefsen KN, Concheiro M, Suzuki M, Rice KC, Huestis MA,
574 Baumann MH (2017) Pharmacokinetic Profiles and Pharmacodynamic Effects for Methylone and Its
575 Metabolites in Rats. Neuropsychopharmacology 42:649–660.

576 Homayoun H, Moghaddam B (2007) NMDA receptor hypofunction produces opposite effects on
577 prefrontal cortex interneurons and pyramidal neurons. J Neurosci 27:11496–11500.

578 Hu S (2016) Listening to the Brain With Photoacoustics. IEEE J Select Topics Quantum Electron
579 22:117–126.

580 Hu S, Wang LV (2010) Neurovascular photoacoustic tomography. Front Neuroenergetics 2:10.

581 Hui J, Cao Y, Zhang Y, Kole A, Wang P, Yu G, Eakins G, Sturek M, Chen W, Cheng J-X (2017) Real-
582 time intravascular photoacoustic-ultrasound imaging of lipid-laden plaque in human coronary artery
583 at 16 frames per second. Sci Rep 7:1417.

584 Huynh E, Jin CS, Wilson BC, Zheng G (2014) Aggregate enhanced trimodal porphyrin shell
585 microbubbles for ultrasound, photoacoustic, and fluorescence imaging. Bioconjugate Chem 25:796–
586 801.

587 Ju K-Y, Kang J, Pyo J, Lim J, Chang JH, Lee J-K (2016) pH-Induced aggregated melanin nanoparticles
588 for photoacoustic signal amplification. Nanoscale 8:14448–14456.

589 Kang J, Chung WY, Kang S-W, Kwon HJ, Yoo J, Kim E-K, Chang JH, Song T-K, Lee S, Kwak JY
590 (2014) Ex Vivo Estimation of Photoacoustic Imaging for Detecting Thyroid Microcalcifications
591 Chen X, ed. PLoS ONE 9.

592 Kang J, Kim E-K, Kim GR, Yoon C, Song T-K, Chang JH (2015) Photoacoustic imaging of breast
593 microcalcifications: a validation study with 3-dimensional ex vivo data and spectrophotometric
594 measurement. J Biophoton 8:71–80.

595 Kang J, Zhang HK, Kadam SD, Fedorko J, Valentine H, Kang JU, Rahmim A, Gjedde A, Loew LM,
596 Wong DF, Boctor EM (2017) Transcranial real-time *in vivo* recording of electrophysiological neural
597 activity in the rodent brain with near-infrared photoacoustic voltage-sensitive dye imaging.
598 BioRxiv:1–23.

599 Kang SK, Ammanuel S, Thodupunuri S, Adler DA, Johnston MV, Kadam SD (2018) Sleep dysfunction
600 following neonatal ischemic seizures are differential by neonatal age of insult as determined by
601 qEEG in a mouse model. Neurobiol Dis 116:1–12.

602 Kim GR, Kang J, Kwak JY, Chang JH, Kim SI, Youk JH, Moon HJ, Kim MJ, Kim E-K (2014)
603 Photoacoustic imaging of breast microcalcifications: a preliminary study with 8-gauge core-biopsied
604 breast specimens. Woloschak GE, ed. PLoS ONE 9:e105878.

605 Kondo M, Kobayashi K, Ohkura M, Nakai J, Matsuzaki M (2017) Two-photon calcium imaging of the
606 medial prefrontal cortex and hippocampus without cortical invasion. Elife 6:592.

607 Krnjević K (1997) Role of GABA in cerebral cortex. Can J Physiol Pharmacol 75:439–451.

608 Li W, Chen R, Lv J, Wang H, Liu Y, Peng Y, Qian Z, Fu G, Nie L (2018) In Vivo Photoacoustic
609 Imaging of Brain Injury and Rehabilitation by High-Efficient Near-Infrared Dye Labeled
610 Mesenchymal Stem Cells with Enhanced Brain Barrier Permeability. Adv Sci (Weinh) 5:1700277–11.

611 Liu Y, Yang Y, Sun M, Cui M, Fu Y, Lin Y, Li Z, Nie L (2017) Highly specific noninvasive
612 photoacoustic and positron emission tomography of brain plaque with functionalized croconium dye
613 labeled by a radiotracer. Chem Sci 8:2710–2716.

614 Luke GP, Yeager D, Emelianov SY (2011) Biomedical Applications of Photoacoustic Imaging with
615 Exogenous Contrast Agents. Ann Biomed Eng 40:422–437.

616 Marrannes R, Willems R, De Prins E, Wauquier A (1988) Evidence for a role of the N-methyl-D-
617 aspartate (NMDA) receptor in cortical spreading depression in the rat. Brain Res 457:226–240.

618 McCormick DA (1989) GABA as an inhibitory neurotransmitter in human cerebral cortex. Journal of
619 Neurophysiology 62:1018–1027.

620 Medina-Ceja L, Pardo-Peña K, Morales-Villagrán A, Ortega-Ibarra J, López-Pérez S (2015) Increase in
621 the extracellular glutamate level during seizures and electrical stimulation determined using a high
622 temporal resolution technique. BMC Neurosci 16:11.

623 Moon H, Kang J, Sim C, Kim J, Lee H, Chang JH, Kim H (2015) Multifunctional theranostic contrast
624 agent for photoacoustics- and ultrasound-based tumor diagnosis and ultrasound-stimulated local
625 tumor therapy. Journal of Controlled Release 218:63–71.

626 Moon J-M, Thapliyal N, Hussain KK, Goyal RN, Shim Y-B (2018) Conducting polymer-based
627 electrochemical biosensors for neurotransmitters: A review. Biosens Bioelectron 102:540–552.

628 Nie L, Cai X, Maslov K, Garcia-Uribe A, Anastasio MA, Wang LV (2012) Photoacoustic tomography
629 through a whole adult human skull with a photon recycler. J Biomed Opt 17:110506.

630 Okubo Y, Sekiya H, Namiki S, Sakamoto H, Iinuma S, Yamasaki M, Watanabe M, Hirose K, Iino M
631 (2010) Imaging extrasynaptic glutamate dynamics in the brain. Proceedings of the National Academy
632 of Sciences 107:6526–6531.

633 Paxinos G, Watson C (2014) The Rat Brain in Stereotaxic Coordinates, Seventh edition. Elsevier
634 Academic Press. Available at:
635 https://books.google.com/books?id=FuqGAwAAQBAJ&printsec=frontcover#v=onepage&q&f=
636 false.

637 Petersen CC, Sakmann B (2001) Functionally independent columns of rat somatosensory barrel cortex
638 revealed with voltage-sensitive dye imaging. J Neurosci 21:8435–8446.

639 Petersen CCH, Grinvald A, Sakmann B (2003) Spatiotemporal Dynamics of Sensory Responses in Layer
640 2/3 of Rat Barrel Cortex Measured In Vivo by Voltage-Sensitive Dye Imaging Combined with
641 Whole-Cell Voltage Recordings and Neuron Reconstructions. Journal of Neuroscience 23:1298–
642 1309.

643 Rao B, Zhang R, Li L, Shao J-Y, Wang LV (2017) Photoacoustic imaging of voltage responses beyond
644 the optical diffusion limit. Sci Rep 7:2560.

645 Roberts S, Seeger M, Jiang Y, Mishra A, Sigmund F, Stelzl A, Lauri A, Symvoulidis P, Rolbieski H,
646 Preller M, Deán-Ben XL, Razansky D, Orschmann T, Desbordes SC, Vetschera P, Bach T,
647 Ntziachristos V, Westmeyer GG (2018) Calcium Sensor for Photoacoustic Imaging. J Am Chem Soc
648 140:2718–2721.

649 Rogawski MA (2013) AMPA receptors as a molecular target in epilepsy therapy. Acta Neurologica
650 Scandinavica 127:9–18.

651 Sachdev RNS, Krause MR, Mazer JA (2012) Surround suppression and sparse coding in visual and barrel
652 cortices. Front Neural Circuits 6:43.

653 Sherman AD, Hegwood TS, Baruah S, Waziri R (1991) Deficient NMDA-mediated glutamate release
654 from synaptosomes of schizophrenics. Biol Psychiatry 30:1191–1198.

655 Szabo GG, Du X, Oijala M, Varga C, Parent JM, Soltesz I (2017) Extended Interneuronal Network of
656 the Dentate Gyrus. Cell Rep 20:1262–1268.

657 Taube JS, Schwartzkroin PA (1987) Hyperpolarizing responses to application of glutamate in
658 hippocampal CA1 pyramidal neurons. Neuroscience Letters 78:85–90.

659 Voets NL, Hodgetts CJ, Sen A, Adcock JE, Emir U (2017) Hippocampal MRS and subfield volumetry at
660 7T detects dysfunction not specific to seizure focus. Sci Rep:1–14.

661 Wang LV, Hu S (2012) Photoacoustic tomography: in vivo imaging from organelles to organs. Science
662 335:1458–1462.

663 Wang X, Pang Y, Ku G, Xie X, Stoica G, Wang LV (2003) Noninvasive laser-induced photoacoustic
664 tomography for structural and functional in vivo imaging of the brain. Nat Biotechnol 21:803–806.

665 Weber J, Beard PC, Bohndiek SE (2016) Contrast agents for molecular photoacoustic imaging. Nat Meth
666 13:639–650.

667 Wu M, Springeling G, Lovrak M, Mastik F, Iskander-Rizk S, Wang T, van Beusekom HMM, van der
668 Steen AFW, Van Soest G (2017) Real-time volumetric lipid imaging in vivo by intravascular
669 photoacoustics at 20 frames per second. Biomed Opt Express 8:943–953.

670 Yao J, Maslov KI, Wang LV (2012) In vivo Photoacoustic Tomography of Total Blood Flow and
671 Potential Imaging of Cancer Angiogenesis and Hypermetabolism. Technol Cancer Res Treat 11:301–
672 307.

673 Young AM, Bradford HF (1991) N-methyl-D-aspartate releases excitatory amino acids in rat corpus
674 striatum in vivo. J Neurochem 56:1677–1683.

675 Zhang HF, Maslov K, Stoica G, Wang LV (2006) Functional photoacoustic microscopy for high-
676 resolution and noninvasive in vivo imaging. Nat Biotechnol 24:848–851.

677 Zhang HK, Yan P, Kang J, Abou DS, Le HND, Jha AK, Thorek DLJ, Kang JU, Rahmim A, Wong DF,
678 Boctor EM, Loew LM (2017) Listening to membrane potential: photoacoustic voltage-sensitive dye
679 recording. J Biomed Opt 22:045006.

680 Zhang P, Li L, Lin L, Hu P, Shi J, He Y, Zhu L, Zhou Y, Wang LV (2018) High-resolution deep
681 functional imaging of the whole mouse brain by photoacoustic computed tomography in vivo. J
682 Biophoton 11:e201700024–e201700026.

683